

Author Manuscript

Title: Semiclassical Trajectory Studies of Reactive and Nonreactive Scattering of OH(A 2S+) by H₂ Based on an Improved Full-Dimensional Ab Initio Diabatic Potential Energy Matrix

Authors: Shanyu Han; Antonio G. S. de Oliveira-Filho; Yinan Shu; Donald G. Truhlar; Hua Guo

This is the author manuscript accepted for publication. It has not been through the copyediting, typesetting, pagination and proofreading process, which may lead to differences between this version and the Version of Record.

To be cited as: 10.1002/cphc.202200039

Link to VoR: <https://doi.org/10.1002/cphc.202200039>

Semiclassical Trajectory Studies of Reactive and Nonreactive Scattering of $\text{OH}(A^2\Sigma^+)$ by H_2 Based on an Improved Full-Dimensional Ab Initio Diabatic Potential Energy Matrix

Dr. Shanyu Han,¹ Prof. Antonio G. S. de Oliveira-Filho,² Dr. Yinan Shu,³ Prof. Donald G. Truhlar,^{3,*} and Prof. Hua Guo^{1,*}

¹*Department of Chemistry and Chemical Biology, University of New Mexico, Albuquerque, NM 87131, USA*

²*Departamento de Química, Laboratório Computacional de Espectroscopia e Cinética, Faculdade de Filosofia, Ciências e Letras de Ribeirão Preto, Universidade de São Paulo, 14040-901, Ribeirão Preto-SP, Brazil*

³*Department of Chemistry, Chemical Theory Center, and Minnesota Supercomputing Institute, University of Minnesota, Minneapolis, Minnesota 55455-0431, USA*

*corresponding authors: truhlar@umn.edu and hguo@unm.edu

ABSTRACT. We present a new full-dimensional diabatic potential energy matrix (DPEM) for electronically nonadiabatic collisions of $\text{OH}(A^2\Sigma^+)$ with H_2 , and we calculate the probabilities of electronically adiabatic inelastic collisions, nonreactive quenching, and reactive quenching to form $\text{H}_2\text{O} + \text{H}$. The DPEM was fitted using a many-body expansion with permutationally invariant polynomials in bond-order functions to represent the many-body part. The dynamics calculations were carried out with the fewest-switches with time uncertainty and stochastic decoherence (FSTU/SD) semiclassical trajectory method. We present results both for head-on collisions (impact parameter b equal to zero) and for a full range of impact parameters. The results are compared to experiment and to earlier FSTU/SD and quantum dynamics calculations with a previously published DPEM. The various theoretical results all agree that nonreactive quenching dominates reactive quenching, but there are quantitative differences between the two DPEMs and between the $b = 0$ results and the all- b results, especially for the probability of reactive quenching.

I. Introduction

The hydroxyl radical (OH) is a key oxidizing agent in combustion and atmospheric chemistry.[1, 2] Its laser-induced fluorescence (LIF) is widely used in flame diagnostics.[3] However, the OH radiative decay from the excited $A^2\Sigma^+$ state can be quenched by collision-induced radiationless transitions to the $X^2\Pi$ ground state, and there is thus strong interest in understanding the competition between the radiative and nonradiative channels. Experimentally, Lester and coworkers have extensively investigated the quenching of $\text{OH}(A^2\Sigma^+)$ by H_2 molecules, and they found that it involves nonadiabatic pathways to both $\text{OH}(X^2\Pi) + \text{H}_2$ (nonreactive quenching) and $\text{H}_2\text{O} + \text{H}$ (reactive quenching).[4-10] The reactive quenching channel was further confirmed by Davis and coworkers.[11] More recently, the electronically elastic scattering back to $\text{OH}(A^2\Sigma^+)$ and H_2 was investigated by Brouard et al.,[12] and it was found to dominate over the quenching channels. Many theoretical studies have been performed to understand the electronic structure of this system and the resulting dynamics.[6, 13-23] The electronic structure studies have produced adiabatic potential energy surfaces (APESs) and diabatic potential energy matrices (DPEMs) in both full and reduced dimensionality,[16-19, 22, 23] and they have paid special attention to conical intersections (CIs), which are seams where adiabatic electronic states are degenerate[24-27] and which identify regions of coordinate space that are especially important for nonradiative decay pathways.[28] The dynamics calculations on these APESs and DPEMs have yielded outcomes that can be directly compared to experimental ones.[16-19, 29]

In a recent theoretical study, the collision dynamics between $\text{OH}(A^2\Sigma^+)$ and H_2 was investigated with a full-dimensional quantum model with zero total angular momentum.[29] These quantum dynamics calculations were based on a four-state DPEM developed recently by Malbon, Zhao, Guo and Yarkony (MZGY),[23] and the general reliability of the DPEM was validated by the calculations reproducing the experimental $\text{OH}(X^2\Pi)$ rovibrational state distributions[8] and the experimental propensity[8] for nonreactive quenching to produce the A' component of the ground-electronic-state Λ -doublet. The calculations are also consistent with the experiment reported by Brouard and coworkers,[12] in that the cross section of electronically elastic, rotationally (in)elastic scattering on the excited-state APES substantially exceeds that for quenching. The new quantum dynamics calculations found the reactive and nonreactive quenching channels to have roughly the same yield,[29] which is consistent with earlier

calculations[19] employing trajectory surface hopping (TSH) on an independently developed DPEM, but this disagrees with an earlier report based on experimental data[7] in which the reactive channel was said to dominate the quenching. It was pointed out[29] that the earlier interpretation of reactive-channel dominance is flawed because the strong coupling to the electronically adiabatic channel was not included in the analysis;[7] when the contribution of the electronically adiabatic channel is included, the theory-experiment agreement was greatly improved.[29]

In the present work, we investigate the OH_3 system using a different dynamics method and a different DPEM. Instead of the quantum treatment, the dynamics is characterized using the fewest switches with time uncertainty and stochastic decoherence (FSTU/SD) method.[30] This method adds time uncertainty[31] and stochastic decoherence[30] to the fewest-switches TSH method of Tully.[32] These dynamics calculations are based on a new DPEM, presented here, which is an improved version of an earlier three-state DPEM,[22] improved by adding more *ab initio* points to provide a more accurate description of the quenching paths and pruning some points with high energies.

The aims of the present study are twofold. First, we compare dynamical results for two DPEMs developed with different *ab initio* and fitting methods. Second, we examine the accuracy of semiclassical methods for treating nonadiabatic dynamics. Semiclassical treatments of nonadiabatic dynamics are important[33-35] because quantum mechanical treatments can hardly go beyond six-dimensions,[36, 37] (although recent progress[38] is encouraging).

This work is organized as follows. Section II provides the details of the electronic structure calculations, fitting, and dynamics calculations. Section III presents the results and discussion. The final section contains conclusions.

II. Methods

II.A. Electronic Structure and Diabatic Potential Energy Matrix

The new DPEM will be called FFW2 to denote that it is version 2 of the fourfold-way DPEM presently previously; we refer the reader to the article^[22] about the original version (which may now be called FFW1) for a detailed discussion of the electronic structure calculations and the construction the global DPEM for the OH_3 system. Here, only a general description is included to present the most important information. The FFW1 matrix is based on *ab initio* calculations performed with extended multiconfiguration quasi-degenerate perturbation

theory[39, 40] (XMC-QDPT). The reference states for the perturbation theory are state-averaged complete active space self-consistent field (SA-CASSCF)[41] wave functions with an active space of 9 active electrons in 11 active orbitals and averaging over 3 electronic states. The basis set on O atom was the cc-pVTZ basis with two additional evenly tempered diffuse *s* and *p* subshells, and the basis set on the H atom is unaugmented cc-pVTZ. The adiabatic-to-diabatic transformation was carried out by the fourfold way based on diabatic molecular orbitals and configuration uniformity.[42-46] This yielded a 3×3 symmetric DPEM with smoothly varying matrix elements U_{jk} , whose six independent elements (U_{11} , U_{22} , and U_{33} are the diabatic surfaces, and U_{12} , U_{23} , and U_{13} are the diabatic couplings) are fit with permutationally invariant polynomials of mixed exponential–Gaussian functions with only connected terms. The APESs are the eigenvalues of the DPEM, and nonadiabatic coupling vectors are obtained from the eigenanalysis of the DPEM using general formulas presented previously.[47]

The FFW2 DPEM is closely related to the previously described FFW1; the only significant differences are changes in the dataset used for fitting as described next.

The dataset of ref. [22] was pruned by the following iterative procedure based on a committee of neural networks. We first fit all the available data with 20 neural networks. Geometries where DPEM elements had errors higher than ten times the average root-mean-square error (RMSE) for ten or more neural-network fits were removed from the database (these are mainly points with very high energies that are hard to fit because of their high energies but also unnecessary to fit because of their high energies). This procedure was repeated with smaller and smaller datasets until the RMSE converged and smooth fits were obtained. Note that the pruned points were removed for refitting (as described below) the diagonal matrix elements (the diabatic potentials) of the DPEM, but we did not need to remove them for refitting the off-diagonal elements (the diabatic couplings). Eventually about 10% of the points were removed.

Then the dataset was augmented by the inclusion of 197 new data points. These new points are all for planar arrangements of interacting fragments in their equilibrium ground state geometries. Using the coordinates defined in Figure 1(a), the first 167 of these points are two-dimensional cuts in which the distance R between the centers of mass of OH and H₂ varies from 1 to 5 Å and the orientation angle of H₂ is between 0.1 and 179.9°, with the OH bond aligned with the line that connects the centers-of-mass of OH and H₂ and the oxygen atom closest to the

H₂ molecule. The remaining 30 points are a one-dimensional cut along the OH orientation angle with R fixed at 2.117 Å.

The final modification of the dataset used for fitting the diabatic potentials was the replacement of the long-range part of the pairwise potential for OH($A^2\Sigma^+$) in the U_{33} diabatic potential by a D3(BJ) damped-dispersion term.[48, 49] This allowed a smooth connection between the OH($A^2\Sigma^+$) short-range potential and the atomization limit, with all atoms in their ground states.

These modifications yielded more accurate database for fitting the DPEM. To fit the DPEM, we have again employed permutation invariant polynomials[50, 51] with only connected terms[52] with the pairwise contribution fitted separately[53] (so the polynomials are used only for the three- and four-body parts), and with mixed exponential-Gaussian (MEG) variables.[54, 55] See the original fitting paper^[22] for a detailed description of choice of parameters of MEG function. The fits for U_{11} , U_{22} , and U_{33} are based on 57698, 57818, and 43760 points and have mean unsigned deviations (MUDs) from the fitting data of 0.113, 0.065, and 0.059 eV, respectively.

Then part of the new database was used to improve the permutationally invariant polynomial fits to the diabatic couplings. The fits for U_{12} , U_{13} , and U_{23} had 30773, 81773, and 30387 points respectively. There are two reasons that a larger database was employed in fitting of U_{13} than U_{12} and U_{23} : first, some points were duplicated in the dataset to increase their weight; second, the U_{12} and U_{23} functions have B₁ symmetry and therefore all planar geometries are exactly zero and hence are not included in the database. These points were cleaned by the cluster growing algorithm developed in the process of making the original fit^[22] and used to smooth the phases of off-diagonal matrix elements, so they are suitable for fitting with continuous functions. The MUDs for the current fitting of U_{12} , U_{13} , and U_{23} are 0.093, 0.104, and 0.081 eV, respectively.

II.B. Semiclassical nonadiabatic dynamics

The nonadiabatic dynamics of the OH($A^2\Sigma^+$) + H₂ collisions were investigated with the FSTU/SD TSH method as implemented in the *Adiabatic and Non-adiabatic Trajectories* (ANT)[56] package. The trajectories were propagated by solving Hamilton's equation in the adiabatic representation. The initial coordinates and momenta of the atoms were sampled from the rovibrational ground state of the OH($A^2\Sigma^+$) and H₂ reactants using the harmonic oscillator

approximation. About 80000 trajectories each were propagated for the three collision energies, 0.05, 0.16, and 0.3 eV (the same as used for earlier FSTU/SD calculations[29] based on the MZGY DEPM), and the impact parameter b was randomly sampled with $b_{\max} = 5.5 \text{ \AA}$. In addition, another 25000 trajectories were propagated for the same energies but with b set to zero, so that the results can be compared to the previous study[29] of head-on collisions.

The branching fraction for each channel is determined by the fraction, N_i/N_{tot} , where N_i and N_{tot} are the numbers of trajectories that end in channel i and the total number of trajectories. The corresponding statistical error is given as a fractional error by

$$\Delta_i = \sqrt{(N_{\text{tot}} - N_i) / (N_{\text{tot}} N_i)}.$$

The final rotational and vibrational state distributions of OH($X^2\Pi$) and H₂ products were determined by their rotational angular momenta j , and by using the Einstein-Brillouin-Keller (EBK) method[57] to assign vibrational quantum numbers v (which are continuously distributed in the trajectories), respectively. Here, the electronic and spin angular momenta of the open-shell OH species are ignored. Conventional histogram binning[58] was used to assign them to quantized values of the quantum numbers. For the ground state OH product, the A' and A'' components are summed in calculating the rovibrational distributions.

III. Results

Using the standard convention, the ground adiabatic electronic state of H₃O is labeled \tilde{X} . This is a doublet, and the two lowest-energy excited doublets are called \tilde{A} and \tilde{B} in order of increasing energy. For planar geometries in the entrance channel, these three states have symmetries $^2A'$, $^2A''$, and $^2A'$, respectively. The ground-state of OH is doubly degenerate ($X^2\Pi$) and in interaction with nondegenerate H₂ it connects to the \tilde{X} and \tilde{A} states, and therefore collisions OH in the first excited state ($A^2\Sigma^+$) enter the interaction region on the \tilde{B} surface. The reactive product (H₂O + H) is nondegenerate and is connected to the \tilde{X} state. Therefore, reactive quenching requires a \tilde{B} to \tilde{X} transition, which can be a single transition or stepwise (\tilde{B} to \tilde{A} to \tilde{X}), whereas nonreactive quenching requires a transition from \tilde{B} to either \tilde{X} or \tilde{A} .

As discussed previously,[20, 21] there are two accessible CI seams, one between \tilde{B} and \tilde{A} and another between \tilde{A} and \tilde{X} , and most nonadiabatic transitions are expected to occur in the vicinities of these seams. Both CI seams have the HO...H₂ orientation, i.e., the O is pointing to the H₂. Panels (b) and (c) of Figure 1 show the three APESs as functions of the OH-H₂

coordinate R and either the in-plane orientation angle of OH, θ_{OH} , or the out-of-plane angle, ϕ . Both of these panels show the \tilde{B}/\tilde{A} and \tilde{A}/\tilde{X} intersection regions. In the OH \cdots H₂ orientation, however, there is a van der Waals well that has a barrier to accessing the HO \cdots H₂ CIs; this barrier is shown in panel (e). Panel (d) shows that the \tilde{B}/\tilde{A} and \tilde{A}/\tilde{X} intersection seams have a higher energy for C_{2v} geometries than for $C_{\infty v}$ geometries. These features of the current DPEM are consistent with those of the MZGY DPEM.[23]

The topography of the APESs make one expect that nonadiabatic transitions are more likely to take place in the HO \cdots H₂ orientation. Figure 2 illustrates the relative orientations of the two diatoms when the transitions from the upper state take place, and it shows that the dynamics calculations conform to this expectation. In particular, we see that most trajectories hop from the highest adiabatic (state 3) to the lower adiabatic states (states 1 and 2) near the linear ($C_{\infty v}$) geometries with O pointing to H₂ (θ_{OH} and θ_{H_2} both near 0), as expected, with a smaller number near C_{2v} geometries (θ_{OH} near 0 and θ_{H_2} near 90 deg). Collisions with the H₂ \cdots HO orientation (θ_{OH} near 180 deg) enter the van der Waals well, which provides no access to the nonadiabatic transitions.

We conclude that the fate of OH($A^2\Sigma^+$) + H₂ collisions on the FFW2 surfaces is determined by stereodynamics, in agreement with the earlier conclusion based the MZGY surfaces.[29] When OH approaches H₂ with its H end, the products are scattered electronically adiabatically on the \tilde{B} state back to the OH($A^2\Sigma^+$) + H₂ asymptote. When OH attacks H₂ with its O end, it accesses the CIs and some of the trajectories will make the transitions to the \tilde{A} and \tilde{X} states, leading to either the nonreactive (OH($X^2\Pi$) + H₂) or the reactive (H + H₂O) quenching channels. The branching fractions of the three channels are listed in Table I, in which the previous results using the MZGY DPEM[29] are also listed for comparison. Both the present and the previous TSH calculations employ the FSTU/SD method for surface hopping so the difference in trajectory results is entirely from the DPEM. From the table, we can see the branching fraction at zero impact parameter ($b = 0$) calculated using the FFW2 DPEM is about 0.5 ± 0.1 for the electronically adiabatic scattering which is consistent with the recent work on the MZGY DPEM.[29] When the impact parameter increases, it is harder to reach the crossing seams due to the increasing centrifugal potential. As a result, the adiabatic branching fraction becomes larger

(~0.9). This is consistent with the recent experimental study of Brouard et al.[12] which reported more than 75% of the $\text{OH}(A^2\Sigma^+) + \text{H}_2$ collision outcomes are electronically adiabatic. We note that such strong dependence of the potential topography on the OH orientation is also seen in the quenching of $\text{OH}(A^2\Sigma^+)$ by heavy rare gas atoms.[59, 60]

The calculated branching fractions for the two quenching channels are similar on the current DPEM and the MZGY DPEM, and for $b = 0$ both DPEMs show a preference of a factor between 3.1 and 3.9 for nonreactive quenching, which is remarkably good agreement of the results for the two independently created potential sets. However, although both DPEMs still favor nonreactive scattering when all impact parameters are included, and the ratios are no longer in agreement, with a ratio of 2.3 for FFW2 and a ratio of 6.1 for MZGY. In Figure 3, the branching fractions for the three channels are plotted as functions of the impact parameter, which shows the convergence with respect to b . In the same figure, the results from the FFW2 and MZGY DPEMs are compared, and they behave in a similar way. The preference for nonreactive quenching was also reported in an early TSH study on another DPEM by Collins and coworkers.[19] They studied collisions of $\text{OH}(A^2\Sigma^+)$ with D_2 at collision energies of 0.06–0.20 eV and found the ratio of nonreactive to reactive quenching varied in the range of about 7–8 for $b = 0$ collisions and in the range 4–5 when all b were included. Note that 4–5 is in somewhat higher than the 2.3–3.4 range found for the FFW2 DPEM in their energy range. They also found appreciable quenching to $\text{OD}(X^2\Pi)$, which is reactive exchange quenching, as opposed to reactive abstraction quenching. In the present work, the reactive exchange quenching is considered to be part of the nonreactive quenching since it is indistinguishable in the absence of isotopic substitution. (Nevertheless, we can analyze for this outcome, and we found in the present work for $b = 0$ that 237 out of 25000 trajectories exchanged.)

To examine the performance of the semiclassical TSH method in describing the product state distributions, we compare in Figure 4 the rotational and vibrational distributions of the $\text{OH}(X^2\Pi)$ product in the nonreactive quenching channel using the MZGY DPEM with zero impact parameter ($b = 0$) to the quantum results.[29] The rotational distribution is for vibrational quantum number v equal to 0, while the vibrational distribution was summed over all rotational states. While the agreement between the quantum and semiclassical vibrational distributions is almost quantitative, there are significant differences in the rotational distributions. The quantum mechanical rotational distribution has a peak at rotational quantum number $j = 17$,[29] in good

agreement with experiment[8] (although it is not necessarily meaningful to compare $b = 0$ results to experiment), but the TSH distribution is cooler, with a peak at $j = 8$. Since the quantum and semiclassical results in this figure were computed with the same DPEM, the difference is attributed to quantum effects that are not captured well by the FSTU/SD calculations.

Figure 5 compares the calculated (with all impact parameters) post-collision vibrational distribution of $\text{OH}(X^2\Pi)$ and H_2 in the nonreactive quenching to experiment and previous theory. The OH vibrational distribution has significant excited-state populations, but is dominated by its ground vibrational state, which may be attributed to the OH bond length not changing much in the quenching process through the CI seams. This is consistent with the experiment[8] and with our previous theory.[29] However, the current DPEM appears to overestimate the vibrational excitation, which suggests that the DPEM probably needs further improvement. For H_2 , the vibrational excitation is more pronounced, due apparently to the stretching of the H-H bond near the CI seam. For this product, there is good agreement with that obtained[29] with the MZGY DPEM at the two lower energies, but not at the highest energy.

Figure 6 displays the distributions in the $b = 0$ calculations of the OH and HH bond lengths at the time of downward nonadiabatic transitions from the \tilde{B} state. It shows that most OH bond lengths are in the range $r_{\text{OH}} = 0.85\text{--}1.2 \text{ \AA}$, which is an interval around the equilibrium bond length ($r_{\text{OH}} = 0.97 \text{ \AA}$) for $\text{OH}(X^2\Pi)$. However, the H-H internuclear distance varies in the range $0.5\text{--}1.6 \text{ \AA}$, which represents a larger spread from the equilibrium geometry ($r_{\text{H}_2} = 0.74 \text{ \AA}$).

Figure 7 shows the calculated rotational distribution of the $\text{OH}(X^2\Pi, v = 0)$ product and the $\text{H}_2 (v = 0)$ product for collisions in which OH is nonreactively quenched. The two DPEMs yielded roughly the same inverted distributions, a peak at around $j = 12$. The agreement with experiment[8] is not quantitative. As discussed above, the TSH rotational distribution underestimates the quantum rotational excitation for $b = 0$, so the lower peak in the TSH distribution as compared to the experimental peak is likely due to errors introduced in the semiclassical treatment of the nonadiabatic dynamics. The rotational excitation for the $\text{OH}(X^2\Pi)$ product can be rationalized by the anisotropy on the \tilde{A} and \tilde{X} PESs, which can be clearly seen in Figure 1. We note in passing that the rotational distribution obtained from trajectories starting at the CI seam were shown to have significant excitations in $\text{OH}(X^2\Pi)$, [9, 18] suggesting the rotational excitation is mostly from the \tilde{X} PES. The $\text{OH}(X^2\Pi)$ rotational excitation on the current

DPEM is slightly higher than that on the MZGY DPEM, indicating a stronger torque exerted on the incipient OH.

There is also significant rotational excitation in the H₂ product, as shown in Figure 7. The distribution appears to be cooler than that of the OH product. The agreement between the two DPEMs is quite reasonable. Similar to the OH rotation, the excitation in the H₂ rotation can be attributed to the potential anisotropy in the nonreactive quenching channel. Unfortunately, there are no experimental data with which to compare.

IV. Conclusions

In this work, we report a full-dimensional ab initio DPEM for the OH₃ system, as an improvement of the recently constructed DPEM in ref. [22]. Trajectory surface hopping calculations have been performed to examine the accuracy of this new version for the quenching of OH(A ²Σ⁺) by H₂, and we also calculated the reactive scattering. The main results are generally consistent with the conclusions of the recent dynamics investigation[29] using a different DPEM constructed via a different electronic structure theory and fitting approach,[23] although quantitative differences exist. Specifically, the trajectory surface hopping results on the current DPEM suggest that adiabatic scattering dominates the quenching, and at the lowest energy the trajectory calculations on the two DPEMs predict similar ratios of nonreactive to reactive quenching. Our results also indicate that nonadiabatic transitions are controlled by stereodynamics, occurring as the OH approaches H₂ with its O end. In addition, the OH(X ²Π) vibrational and rotational distributions are consistent with experimental results, although the agreement for the latter is only qualitative. The comparison with quantum results suggest that the semiclassical method for treating state-to-state nonadiabatic collision dynamics is qualitatively and sometimes quantitatively accurate.

Supporting Information. The Supporting Information contains the Fortran code for the FFW2 DPEM, including analytic derivatives and the transformation to the adiabatic representation.

Acknowledgment. This work was supported in part by the U.S. Department of Energy, Office of Science, Office of Basic Energy Sciences under Award Number DE-SC0015997. A.G.S.d.O.-F. acknowledges support from the Conselho Nacional de Desenvolvimento Científico e Tecnológico (CNPq) under Grant No. 306830/2018-3 and the São Paulo Research Foundation

(FAPESP) under Grant No. 2020/08553-2. This study was financed in part by the Coordenação de Aperfeiçoamento de Pessoal de Nível Superior – Brasil (CAPES) – Finance Code 001.

Key words: nonadiabatic dynamics, quenching of OH(A), diabatic potential energy matrix, potential energy surfaces, quantum photochemistry

References

- [1] D. R. Crosley *J. Phys. Chem.* **1989**, *93*, 6273-6282.
- [2] J. H. Lehman, M. I. Lester *Annu. Rev. Phys. Chem.* **2014**, *65*, 537-555.
- [3] D. R. Crosley *ACS Symp. Ser.* **1980**, *134* 3-18.
- [4] D. T. Anderson, M. W. Todd, M. I. Lester *J. Chem. Phys.* **1999**, *110*, 11117-11120.
- [5] M. W. Todd, D. T. Anderson, M. I. Lester *J. Phys. Chem. A.* **2001**, *105*, 10031-10036.
- [6] P. A. Cleary, L. P. Dempsey, C. Murray, M. I. Lester, J. Klos, M. H. Alexander *J. Chem. Phys.* **2007**, *126*, 204316.
- [7] L. P. Dempsey, C. Murray, M. I. Lester *J. Chem. Phys.* **2007**, *127*, 151101.
- [8] L. P. Dempsey, C. Murray, P. A. Cleary, M. I. Lester *Phys. Chem. Chem. Phys.* **2008**, *10*, 1424-1432.
- [9] J. H. Lehman, L. P. Dempsey, M. I. Lester, B. Fu, E. Kamarchik, J. M. Bowman *J. Chem. Phys.* **2010**, *133*, 164307.
- [10] J. H. Lehman, J. L. Bertrand, T. A. Stephenson, M. I. Lester *J. Chem. Phys.* **2011**, *135*, 144303.
- [11] M. Ortiz-Suárez, M. F. Witinski, H. F. Davis *J. Chem. Phys.* **2006**, *124*, 201106.
- [12] M. Brouard, J. Lawlor, G. McCrudden, T. Perkins, S. A. Seamons, P. Stevenson, H. Chadwick, F. J. Aoiz *J. Chem. Phys.* **2017**, *146*, 244313.
- [13] M. I. Lester, R. A. Loomis, R. L. Schwartz, S. P. Walch *J. Phys. Chem. A.* **1997**, *101*, 9195-9206.
- [14] D. R. Yarkony *J. Chem. Phys.* **1999**, *111*, 6661-6664.
- [15] B. C. Hoffman, D. R. Yarkony *J. Chem. Phys.* **2000**, *113*, 10091-10099.
- [16] P.-Y. Zhang, R.-F. Lu, T.-S. Chu, K.-L. Han *J. Phys. Chem. A.* **2010**, *114*, 6565-6568.
- [17] P.-Y. Zhang, R.-F. Lu, T.-S. Chu, K.-L. Han *J. Chem. Phys.* **2010**, *133*, 174316.
- [18] B. Fu, E. Kamarchik, J. M. Bowman *J. Chem. Phys.* **2010**, *133*, 164306.
- [19] M. A. Collins, O. Godsi, S. Liu, D. H. Zhang *J. Chem. Phys.* **2011**, *135*, 234307.
- [20] J. Dillon, D. R. Yarkony *J. Chem. Phys.* **2013**, *139*, 064314.
- [21] J. Dillon, D. R. Yarkony *J. Phys. Chem. A.* **2013**, *117*, 7344-7355.
- [22] Y. Shu, J. Kryven, A. G. Sampaio de Oliveira-Filho, L. Zhang, G.-L. Song, S. L. Li, R. Meana-Pañeda, B. Fu, J. M. Bowman, D. G. Truhlar *J. Chem. Phys.* **2019**, *151*, 104311.
- [23] C. L. Malbon, B. Zhao, H. Guo, D. R. Yarkony *Phys. Chem. Chem. Phys.* **2020**, *22*, 13516-13527.
- [24] E. Teller *J. Phys. Chem.* **1937**, *41*, 109-116.
- [25] D. R. Yarkony *Rev. Mod. Phys.* **1996**, *68*, 985-1013.
- [26] W. Domcke, D. R. Yarkony, H. Köppel, *Conical Intersections: Theory, Computation, and Experiment*, World Scientific, Singapore, **2011**.
- [27] A. W. Jasper, B. K. Kendrick, C. A. Mead, D. G. Truhlar in *Modern Trends in Chemical Reaction Dynamics, Part. I* (Eds.: X. Yang, K. Liu), World Scientific, Singapore, **2004**, pp.329-391.

- [28] E. Teller *Israel J. Chem.* **1969**, *7*, 227-235.
- [29] B. Zhao, S. Han, C. L. Malbon, U. Manthe, D. R. Yarkony, H. Guo *Nat. Chem.* **2021**, *13*, 909-915.
- [30] A. W. Jasper, D. G. Truhlar *J. Chem. Phys.* **2007**, *127*, 194306.
- [31] A. W. Jasper, S. N. Stechmann, D. G. Truhlar *J. Chem. Phys.* **2002**, *116*, 5424-5431.
- [32] J. C. Tully *J. Chem. Phys.* **1990**, *93*, 1061-1071.
- [33] A. W. Jasper, S. Nangia, C. Zhu, D. G. Truhlar *Acc. Chem. Res.* **2006**, *39*, 101-108.
- [34] J. C. Tully *J. Chem. Phys.* **2012**, *137*, 22A301.
- [35] S. Mai, P. Marquetand, L. González *WIREs Comput. Mol. Sci.* **2018**, *8*, e1370.
- [36] J. Li, B. Zhao, D. Xie, H. Guo *J. Phys. Chem. Lett.* **2020**, *11*, 8844-8860.
- [37] Y. Guan, C. Xie, D. R. Yarkony, H. Guo *Phys. Chem. Chem. Phys.* **2021**, *23*, 24962-24983.
- [38] G. Christopoulou, T. Tran, G. A. Worth *Phys. Chem. Chem. Phys.* **2021**, *23*, 23684-23695.
- [39] H. Nakano *J. Chem. Phys.* **1993**, *99*, 7983-7992.
- [40] A. A. Granovsky *J. Chem. Phys.* **2011**, *134*, 214113.
- [41] K. Ruedenberg, L. M. Cheung, S. T. Elbert *Inter. J. Quantum Chem.* **1979**, *16*, 1069-1101.
- [42] K. Ruedenberg, G. J. Atchity *J. Chem. Phys.* **1993**, *99*, 3799-3803.
- [43] H. Nakamura, D. G. Truhlar *J. Chem. Phys.* **2001**, *115*, 10353-10372.
- [44] H. Nakamura, D. G. Truhlar *J. Chem. Phys.* **2002**, *117*, 5576-5593.
- [45] H. Nakamura, D. G. Truhlar *J. Chem. Phys.* **2003**, *118*, 6816-6829.
- [46] S. L. Li, D. G. Truhlar, M. W. Schmidt, M. S. Gordon *J. Chem. Phys.* **2015**, *142*, 064106.
- [47] A. W. Jasper, D. G. Truhlar in *Conical Intersections: Theory, Computation, and Experiment*, (Eds.: W. Domcke, D. R. Yarkony, H. Köppel), World Scientific, Singapore, **2011**, pp375-414.
- [48] S. Grimme, J. Antony, S. Ehrlich, H. Krieg *J. Chem. Phys.* **2010**, *132*, 154104.
- [49] S. Grimme, S. Ehrlich, L. Goerigk *J. Comput. Chem.* **2011**, *32*, 1456-1465.
- [50] B. J. Braams, J. M. Bowman *Int. Rev. Phys. Chem.* **2009**, *28*, 577-606.
- [51] Z. Xie, J. M. Bowman *J. Chem. Theo. Comput.* **2010**, *6*, 26-34.
- [52] Y. Paukku, K. R. Yang, Z. Varga, D. G. Truhlar *J. Chem. Phys.* **2013**, *139*, 044309.
- [53] W. Lin, Z. Varga, G. Song, Y. Paukku, D. G. Truhlar *J. Chem. Phys.* **2016**, *144*, 024309.
- [54] J. D. Bender, P. Valentini, I. Nompelis, Y. Paukku, Z. Varga, D. G. Truhlar, T. Schwartzenuber, G. V. Candler *J. Chem. Phys.* **2015**, *143*, 054304.
- [55] Z. Varga, R. Meana-Pañeda, G. Song, Y. Paukku, D. G. Truhlar *J. Chem. Phys.* **2016**, *144*, 024310.
- [56] J. Zheng, Z.-H. Li, A. W. Jasper, D. A. Bonhommeau, R. Valero, R. Meana-Pañeda, S. L. Mielke, L. Zhang, D. G. Truhlar, ANT (<http://comp.chem.umn.edu/ant>), University of Minnesota, Minneapolis, **2019**.
- [57] M. C. Gutzwiller, *Chaos in Classical and Quantum Mechanics*, Springer, New York, **1990**.
- [58] D. G. Truhlar, J. T. Muckerman in *Atom-Molecule Collision Theory: A Guide for the Experimentalist*, (Ed.: R. B. Bernstein), Plenum, New York, **1979**, pp.505-566.
- [59] T. Perkins, D. Herráez-Aguilar, G. McCrudden, J. Kłos, F. J. Aoiz, M. Brouard *J. Chem. Phys.* **2015**, *142*, 144307.
- [60] J. Kłos, G. McCrudden, M. Brouard, T. Perkins, S. A. Seamons, D. Herráez-Aguilar, F. J. Aoiz *J. Chem. Phys.* **2018**, *149*, 184301.

Table I. Branching fractions for the three product channels.^{a,b}

DPEM	dynamics	$b(\text{\AA})$	E_{rel} (eV)	H+H ₂ O	H ₂ +OH($X^2\Pi$)	N/R ^c	H ₂ +OH($A^2\Sigma^+$)
FFW2	FSTU/SD	0	0.05	0.09	0.33	3.6	0.58
MZGY	FSTU/SD	0	0.05	0.08	0.29	3.9	0.63
MZGY	quantum	0 ^d	0.05	0.10	0.12	1.3	0.77
FFW2	FSTU/SD	0	0.16	0.13	0.44	3.4	0.43
MZGY	FSTU/SD	0	0.16	0.09	0.34	3.8	0.57
MZGY	quantum	0 ^d	0.16	0.11	0.28	2.5	0.61
FFW2	FSTU/SD	0	0.30	0.15	0.45	3.1	0.40
MZGY	FSTU/SD	0	0.30	0.10	0.37	3.7	0.53
MZGY	quantum	0 ^d	0.30	0.19	0.34	1.8	0.48
FFW2	FSTU/SD	≤ 5.5	0.05	0.03	0.06	2.3	0.91
MZGY	FSTU/SD	≤ 5.5	0.05	0.01	0.06	6.1	0.93
FFW2	FSTU/SD	≤ 5.5	0.16	0.02	0.06	3.4	0.92
FFW2	FSTU/SD	≤ 5.5	0.30	0.02	0.06	2.6	0.92

^a The results for the MZGY DPEM are from the study of Zhao et al.[29] E_{rel} denotes the collision energy, i.e., the relative translational energy.

^b In the FSTU/SD calculations, the H+H₂O channel branching fraction has the statistical error (1σ) ranging from 3.5 % for the smallest value (0.009) to 0.9% for the largest value (0.146).

^c Ratio between nonreactive (N) and reactive (R) quenching.

^d The quantum dynamics calculations are actually for zero total angular momentum, but since the diatomics are initially in their zero-angular-momentum ground states, it is reasonable to interpret the quantum calculations as corresponding to impact parameter b equal to 0.

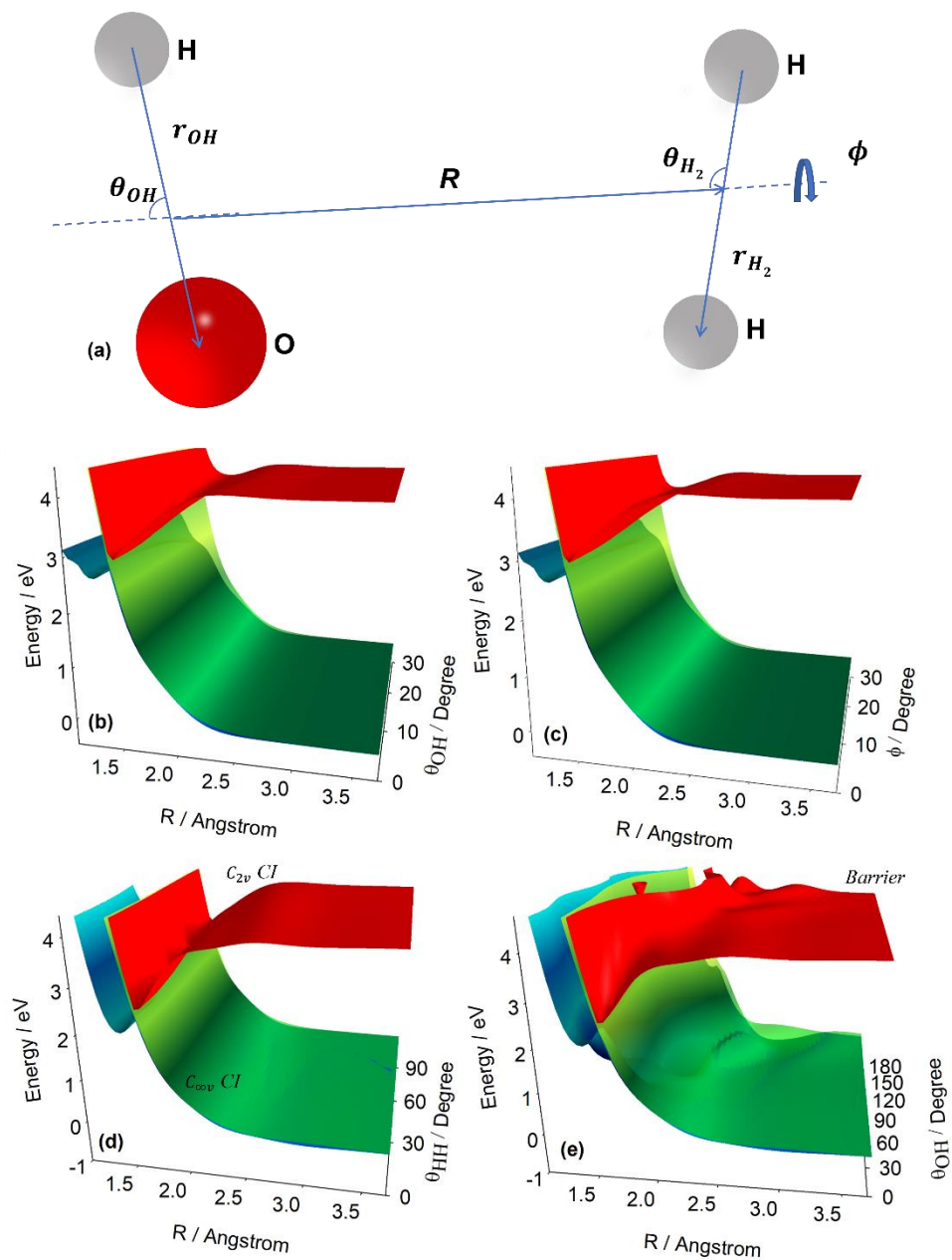


Figure 1. (top \equiv a) The coordinate system. (next two rows) Plots of the three APESs. (second row, left \equiv b) APESs as functions of R and θ_{OH} . (second row, right \equiv c) APESs as functions of R and ϕ . (bottom row, left \equiv d) APES as functions of R and θ_{H_2} . (bottom row, right \equiv e) The same as (b) with $\theta_{H_2} = 0$. For (b) and (c), the H-H bond length is fixed at its equilibrium distance with H₂ perpendicular to the R to maintain C_{2v} symmetry. For (c), the O-H bond length is fixed at its equilibrium value, and the OH orientation is kept with the oxygen pointing to the H₂. Note that at large R , the lowest two adiabatic surfaces are nearly degenerate as they tend to the OH($X^2\Pi$) + H₂ asymptote, and they appear as a single blue surface in the figure.

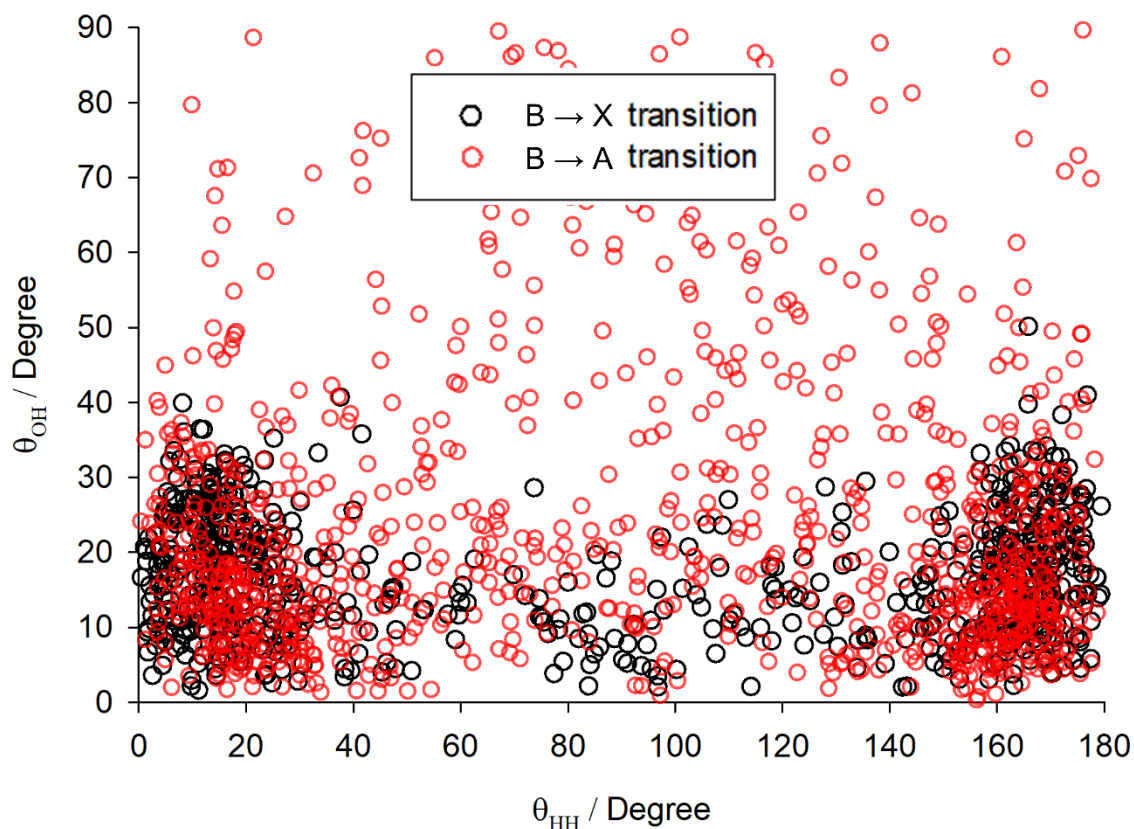


Figure 2. Distribution of the diatomic polar angles (defined in Figure 1(a)) at the \tilde{A} to \tilde{B} transitions in the trajectory surface hopping calculations with the FFW2 DPEM with b sampled within b_{\max} and with a collision energy of 0.3 eV. Note that the distribution would be symmetric upon reflection through $\theta_{H_2} = 90^\circ$ if we had completely converged ensemble averaging; the near symmetry is an indication that ensemble averaging is good enough to draw conclusions.

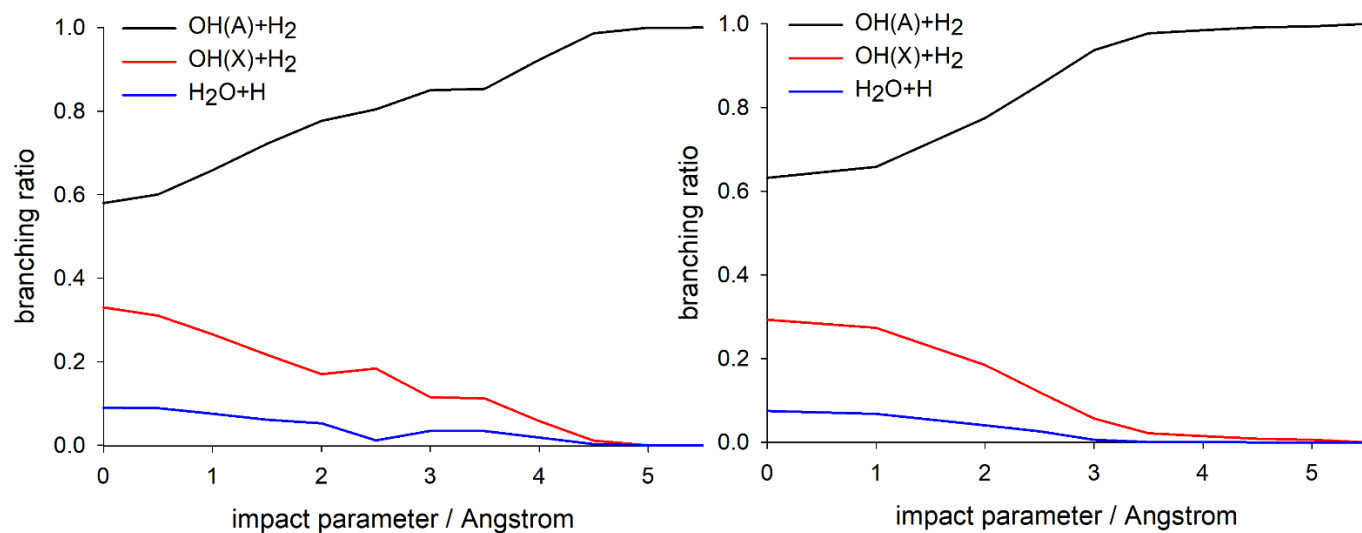


Figure 3. The branching ratios for the OH(A) + H₂ channel, OH(X) + H₂ channel and H₂O + H channel as functions of impact parameter with the FFW2 DPEM (left panel) and the MZGY DPEM (right panel) at 0.05 eV.

Author Manuscript

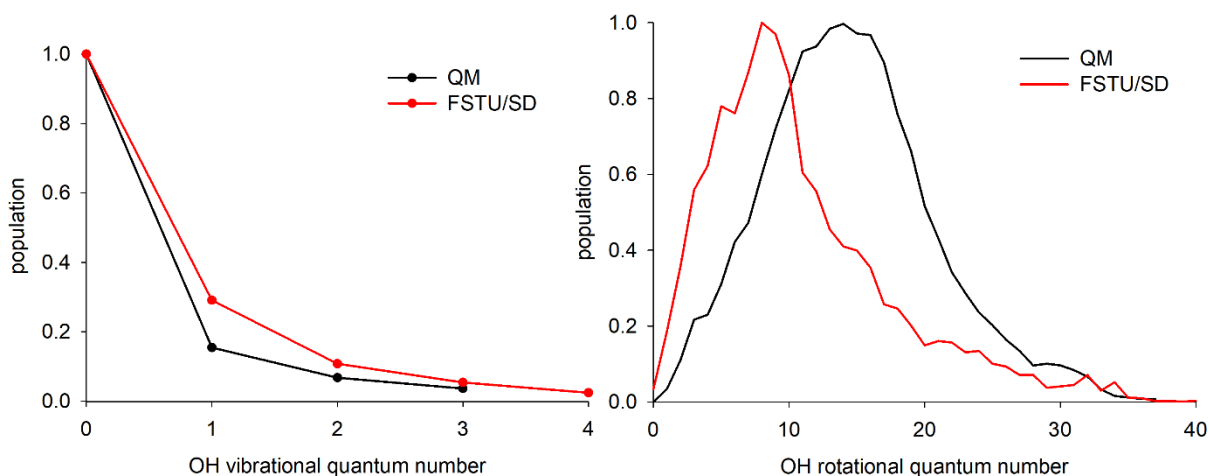


Figure 4. Comparison of the total vibrational distribution and the rotational distributions for $v = 0$ of the $\text{OH}(X^2\Pi)$ product calculated by quantum dynamics[29] and FSTU/SD method. Both calculations were performed on the MZGY DPEM at the collision energy at 0.05 eV and zero impact parameter for FSTU/SD and with zero total angular momentum for quantum dynamics.

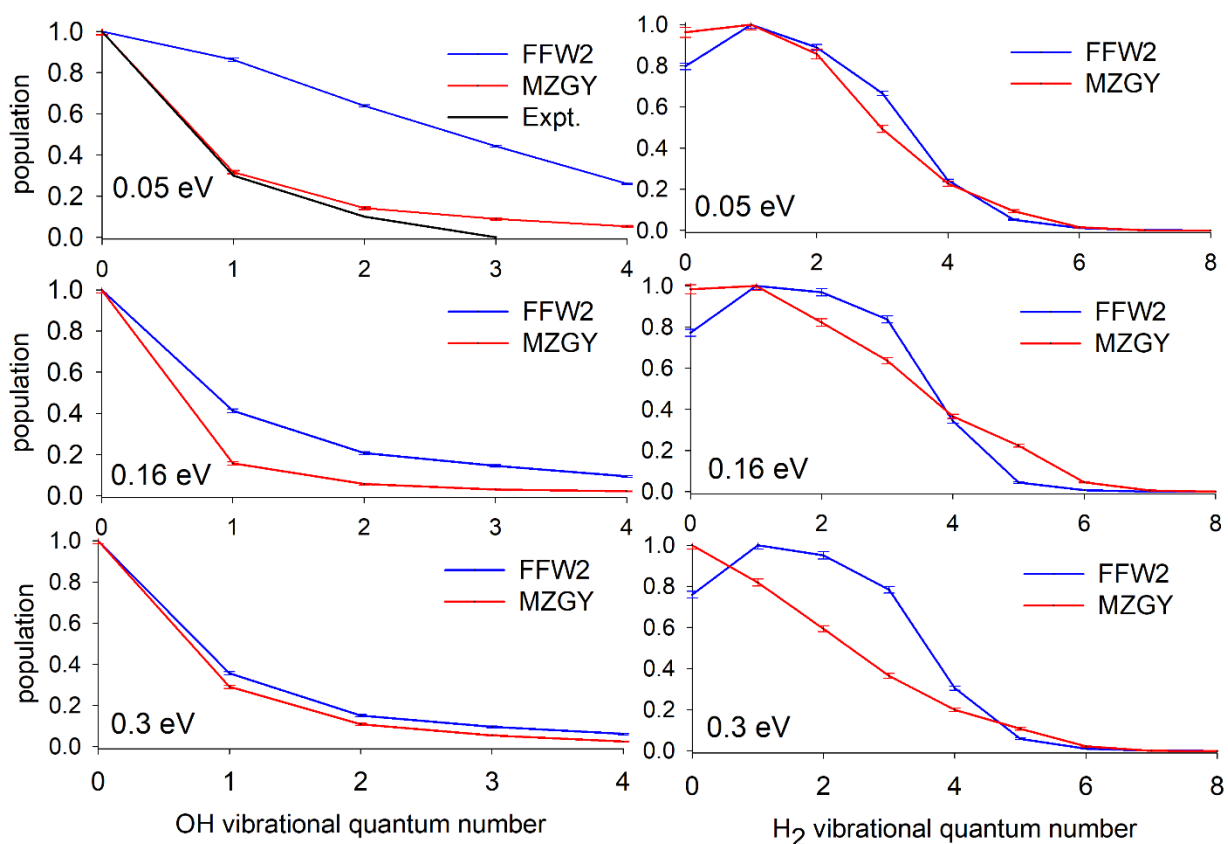


Figure 5. Calculated vibrational distributions of the OH($X^2\Pi$) (left) and H₂ (right) products in the nonreactive quenching channel at the three collision energies using the FFW2 DPEM, and comparison to the TSH results using MZGY DPEM[29] and to the experimental results.[8]

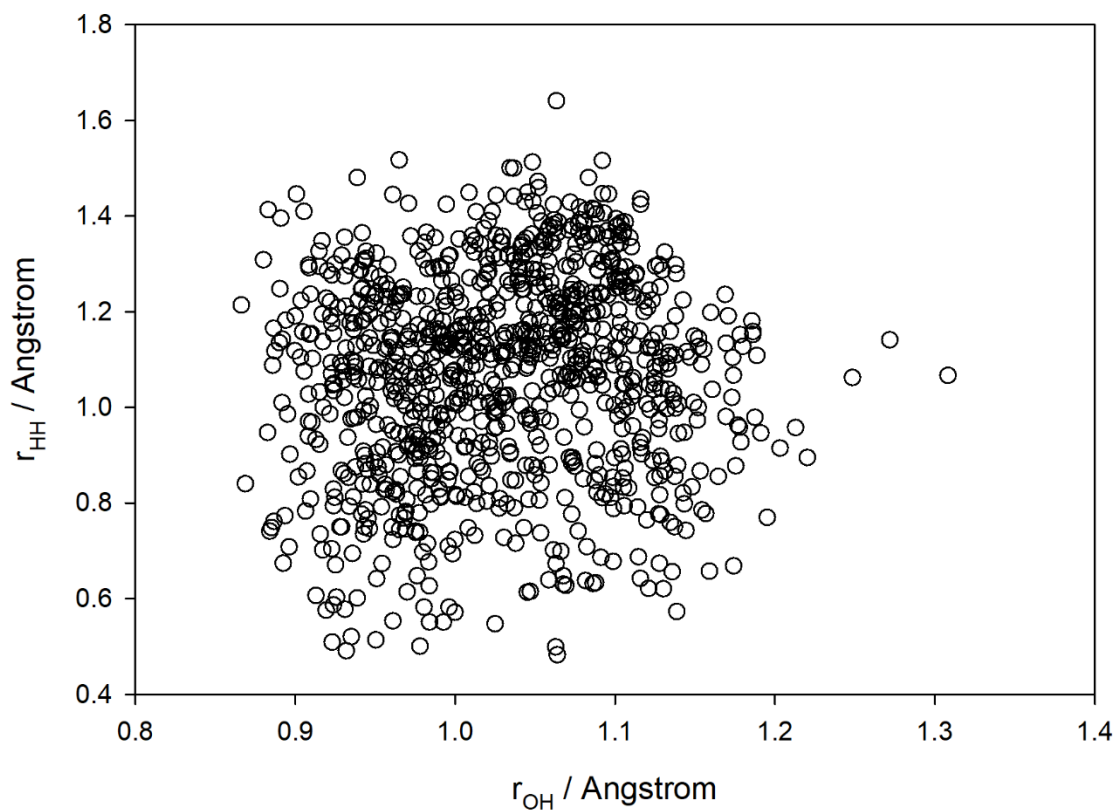


Figure 6. Distributions of the H–H and O–H internuclear distances at the hopping geometries near the $C_{\infty v}$ CI seam (θ_{OH} is restricted to $0\sim 20^\circ$, θ_{HH} is restricted to $0\sim 20^\circ$ or $160\sim 180^\circ$) at the collision energy of 0.05 eV for the calculations with zero impact parameter. The figure includes both hops from \tilde{B} to \tilde{A} and from \tilde{B} to \tilde{X} .

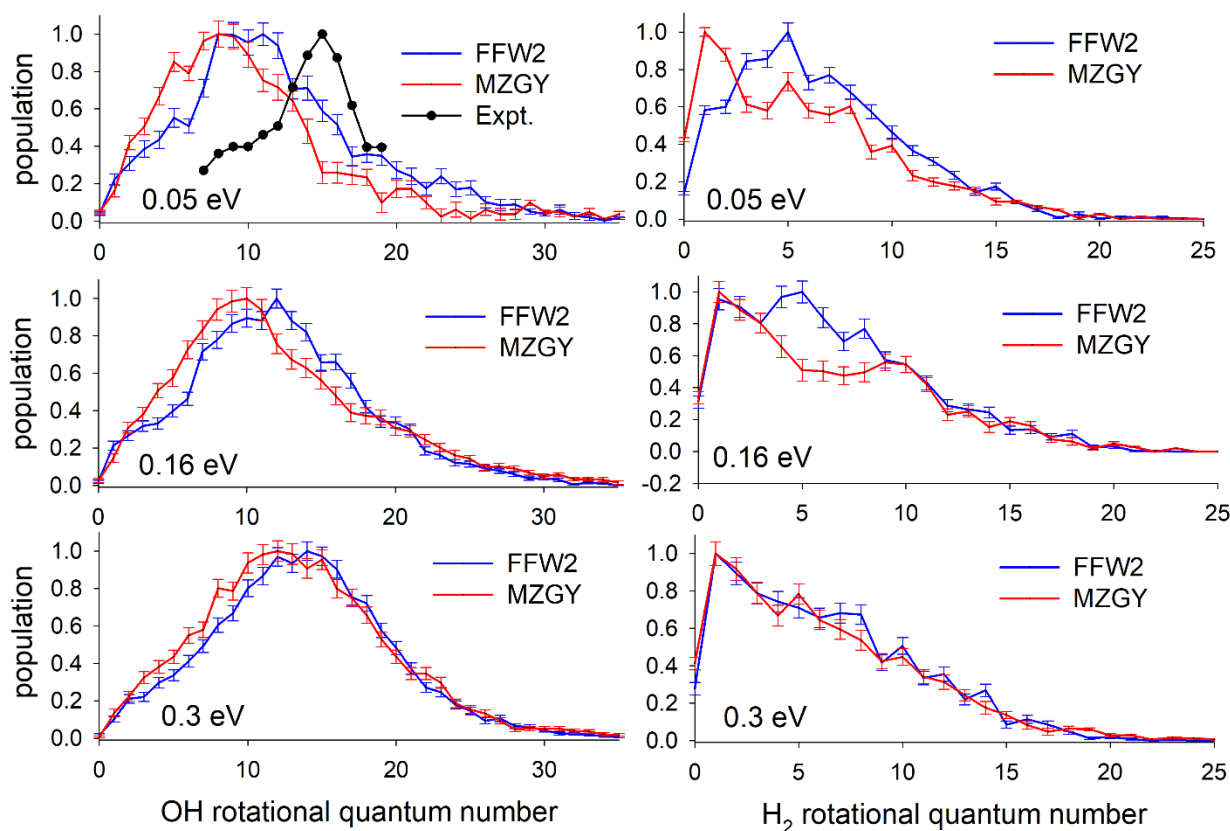
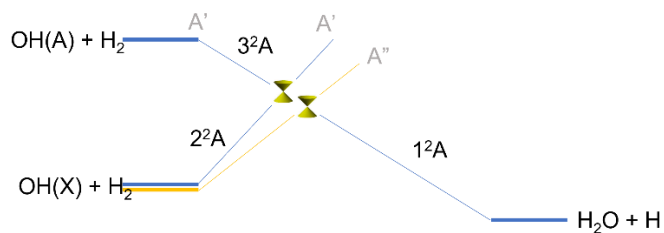


Figure 7. Calculated rotational distributions in the nonreactive quenching channel including all impact parameters at the three collision energies, which are indicated in the lower left portion of each panel. (left) For OH($X^2\Pi$, $\nu=0$ only); (right) For H₂ ($\nu=0$ only). The figure shows FSTU/SD results for both the FFW2 and MZGY DPEMs. One panel also includes the experimental results.[8]

TOC graphic



Semiclassical trajectory calculations for the nonadiabatic quenching of $\text{OH}(\text{A})$ by H_2 on a modified ab initio diabatic potential energy matrix report branching fraction of the adiabatic and nonadiabatic channels and the product internal state distribution in the nonadiabatic quenching channel, in reasonable agreement with experimental and previous quantum calculations.